Mixed-Layer Model Simulation of Eastern North Pacific Stratocumulus

JOSEPH S. WAKEFIELD[1] AND WAYNE H. SCHUBERT

Department of Atmospheric Science, Colorado State University, Fort Collins 80523

(Manuscript received 7 November 1980, in final form 20 April 1981)

ABSTRACT

The cloud-topped mixed-layer theory developed by Lilly (1968) is employed in a slightly generalized form to simulate stratocumulus in the eastern North Pacific. The radiation parameterization involves cloud-top longwave cooling and mixed-layer shortwave heating. Long-wave emissivity and shortwave absorption are functions of cloud thickness. The model is integrated along climatological trajectories which traverse the area bounded by 145°W, 115°W, 20°N and 40°N. The results of the integration include fields of cloud-top and cloud-base height, mixed-layer thermodynamic structure, and convective and radiative fluxes. Where it is possible to compare model-generated fields with the observations of Neiburger *et al.* (1961), general agreement is found. The model-predicted location of the southern limit (due to cloud-top instability) of stratocumulus clouds is in agreement with observations.

1. Introduction

A persistent feature of the atmosphere over the eastern portions of the Pacific and Atlantic oceans is the existence of broad areas of stratocumulus convection capped by a strong inversion. These stratocumulus regimes lie to the east of the large semi-permanent subtropical high pressure centers. That such inversion-capped cloud layers are a persistent feature of the general circulation may be seen by examination of Figs. 1 and 2. Fig. 1 shows the mean relative July cloud cover for 1967–70, as presented by Miller and Feddes (1971). Presented in Fig. 2 are the results of Neiburger *et al.*'s (1961) compilation of observational data, which indicates that inversions exist 80–100% of the time in summer in the region indicated as persistently cloudy in Fig. 1.

The general features of a stratocumulus-topped boundary layer are as follows. Turbulent mixing below the inversion creates a layer in which certain thermodynamic properties are constant with height. In the case of a cloud-topped mixed layer, the well-mixed variables are moist static energy h and total water mixing ratio $q + l$. Since large surface heat fluxes are infrequent in the stratocumulus regimes, the driving mechanism for the convective mixing tends to be the radiational cooling at the top of the mixed layer. Fig. 3 conceptually illustrates the convective mechanism in marine stratocumulus convection. Radiative cooling and the inversion warming and drying (which are caused by large-scale subsidence) lead to turbulent vertical fluxes of heat and moisture at the top of the layer. These fluxes in turn affect the mixed-layer properties, which feed back into both the magnitude of the inversion and the radiative cooling. Mixed-layer temperature and moisture determine the surface fluxes, as well. These surface fluxes feed back into both the mixed layer properties and the cloud-top fluxes, completing the loop.

In order to simulate this phenomenon several classes of models have been developed. The most detailed modeling of cloud-topped boundary layers has been accomplished with a three dimensional numerical model (Deardorff, 1980b). Such a model has the advantage that it eliminates most of the structure assumptions and closure assumptions involved in simpler models. A disadvantage is that the domain size and spatial resolution are severely limited by the amount of computation involved. If one assumes that the convective elements are two-dimensional, it is possible to simulate the marine boundary layer using a two-dimensional model based on the Boussinesq forms of the vorticity and thermodynamic equations, along with the continuity equations for water substance. Such a model has been used by Asai and Nakamura (1978) to investigate air mass transformation over the Kuroshio Current. Another approach to modeling the marine boundary layer involves the use of second-order closure models. Such models have been used to investigate the interaction of turbulent and radiative transport in low-level stratus and fog (Oliver *et al.*, 1978) and the downstream breakup of the stratocumulus regime (Moeng and Arakawa, 1980).

The simplest and most thoroughly studied type of

[1] Present affiliation: PROFS Program Office, NOAA/ERL, Boulder, CO 80303.

0027-0644/81/091952-17$08.25

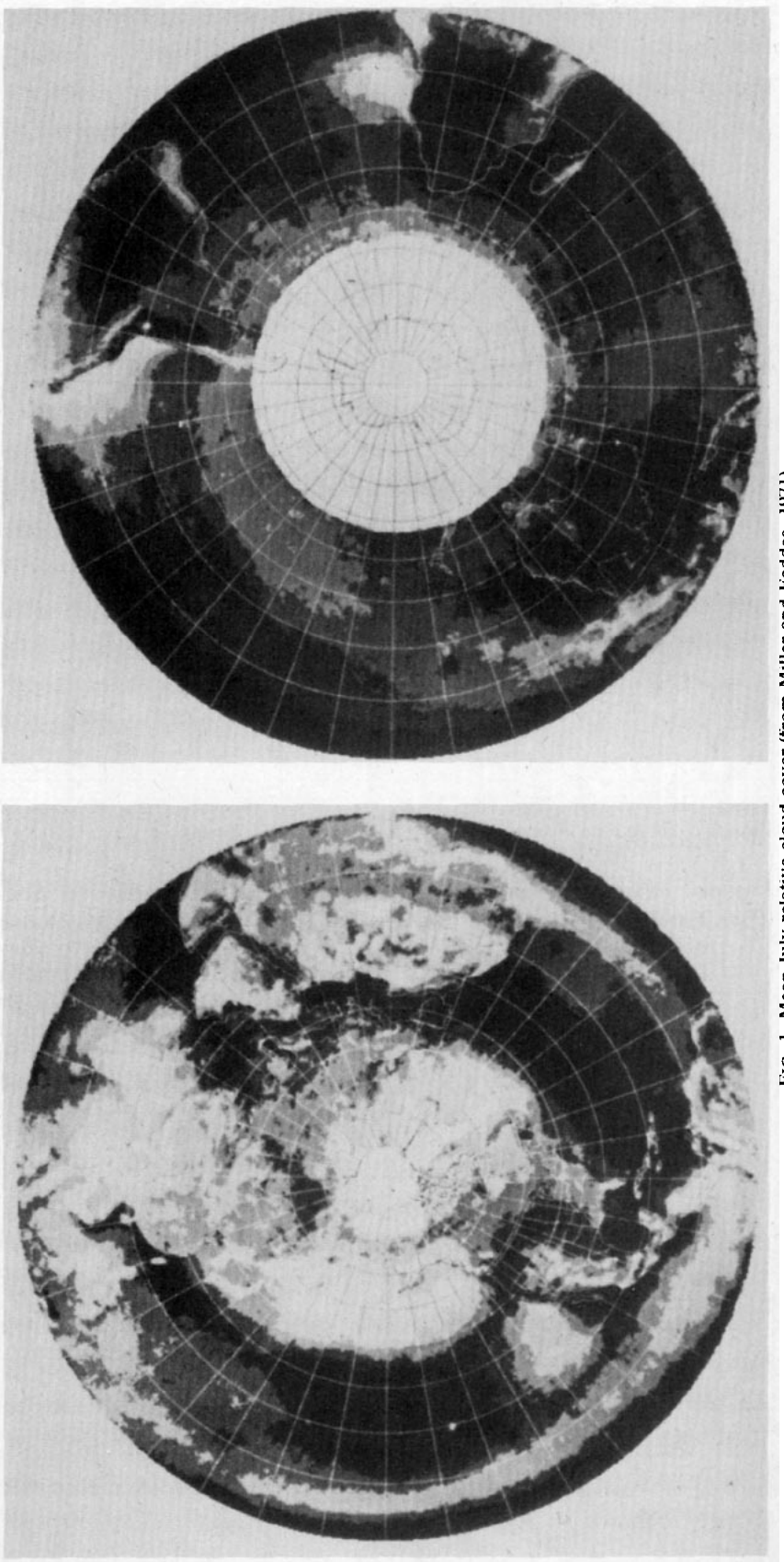

FIG. 1. Mean July relative cloud cover (from Miller and Feddes, 1971).

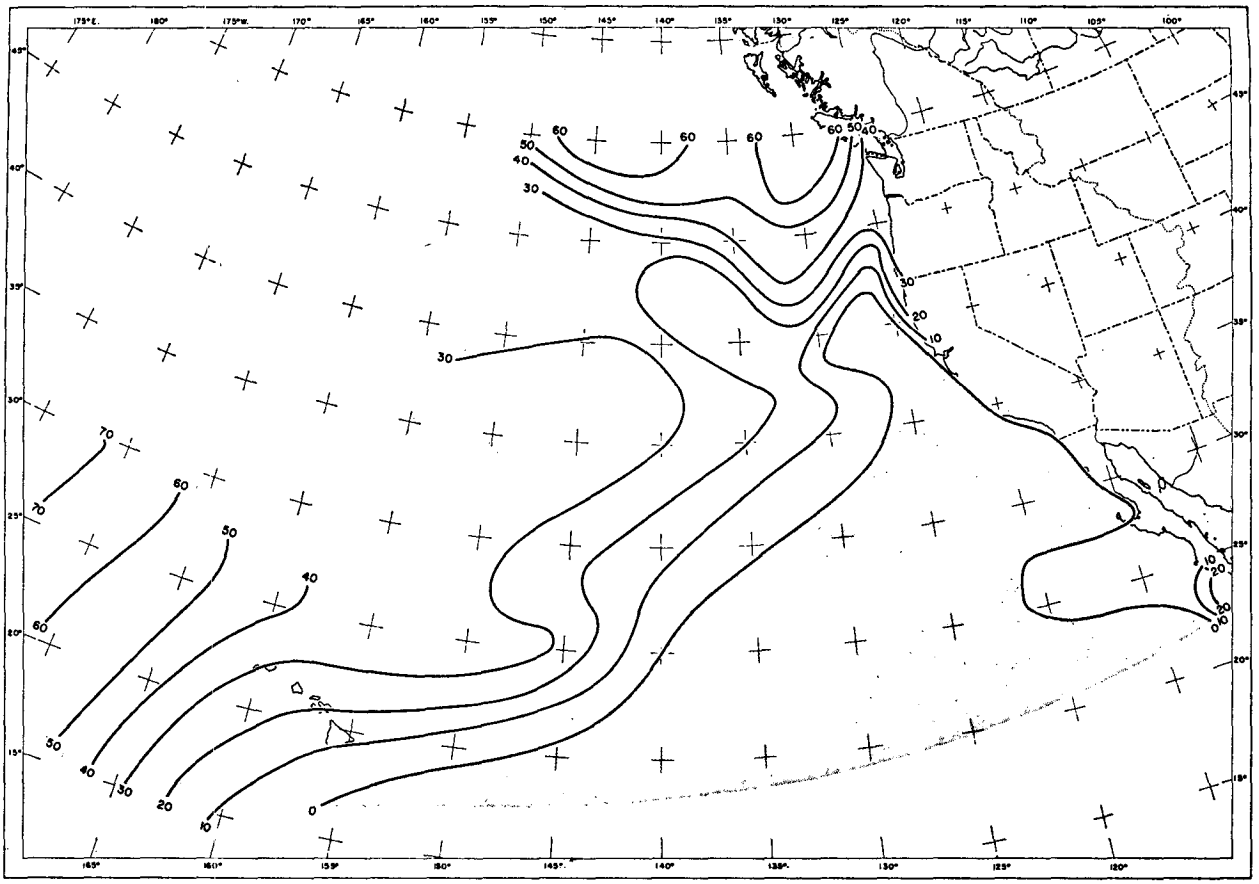

FIG. 2. Percent of observations with no inversion for the period June through September (from Neiburger *et al.*, 1961).

model is the cloud-topped mixed layer model introduced by Lilly (1968). Elaborations and solutions of this model can be found in Schubert (1976), Deardorff (1976), Kraus and Schaller (1978a,b), Schubert *et al.* (1979a,b) and Randall (1980b). Although there remains a lack of consensus on how radiation should be incorporated into the mixed-layer model [cf. formulations of Deardorff (1976), Schubert *et al.* (1979a), Kahn and Businger (1979), Randall (1980b), Deardorff and Businger (1980), Lilly and Schubert (1980), Schaller and Kraus (1981a,b)], there is a general agreement that Lilly's formulation provides a simple and elegant theoretical framework for the study of marine stratocumulus convection. However, in spite of the amount of work with models of the mixed-layer type, there remains the following overlooked aspect. How well does the cloud-topped mixed-layer model reproduce the observed climatological structure of the boundary layer over the eastern ocean? The purpose of this paper is to help answer that question by numerically simulating the stratocumulus convection of the eastern North Pacific and comparing it to the observational evidence of Neiburger *et al.* (1961). The model is presented in Section 2. Section 3 describes the large-scale input fields, and Section 4 the results of the numerical integrations.

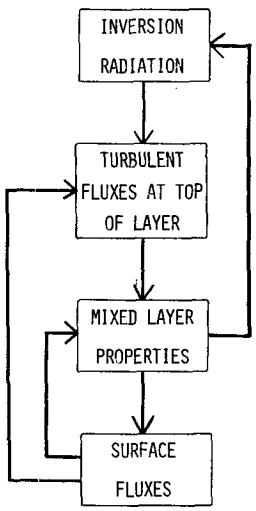

FIG. 3. Conceptual flow diagram of marine stratocumulus convection process.

2. Governing equations

The model employed in this study is similar to that described in Section 3 of Schubert *et al.* (1979a). The only differences are in the radiation parameterization and the bulk aerodynamic transfer coefficient. More detailed discussion of the set of equations may be found in that study, as well as in the project report by Wakefield and Schubert (1978)[2] (hereafter referred to as WS). The first column of Table 1 lists the model's 13 dependent variables, while the second and third columns contain the required constants and externally specified parameters. The dependent variables are functions of the horizontal coordinates and time. We shall use a natural coordinate system in which x denotes distance in the downstream direction. The material derivative d/dt is then given by $\partial/\partial t + V(\partial/\partial x)$, where V is the horizontal wind speed, assumed constant with height.

The model may be written as a set of 13 equations, and is summarized below:

[2] Wakefield, J. S., and W. H. Schubert, 1978: Numerical simulation of eastern North Pacific stratocumulus. Atmos. Sci. Pap. No. 294, Colorado State University, Fort Collins, 115 pp.

$$(\overline{w'h'})_S = C_T V[h_S^* - h_M], \tag{2.1}$$

$$(\overline{w'q'})_S = C_T V[q_S^* - (q + l)_M], \tag{2.2}$$

$$z_C H^{-1} = b^{-1}\{(1 + \gamma)[q_S^* - (q + l)_M] - \gamma L^{-1}[h_S^* - h_M]\}, \tag{2.3}$$

$$\Delta h = h_+ - h_M, \tag{2.4}$$

$$\Delta(q + l) = q_+ - (q + l)_M, \tag{2.5}$$

$$T_B = \frac{1}{c_p}\left[h_M - L(q + l)_M + \frac{Lb}{(1 + \gamma)H}(z_B - z_C) - gz_B\right], \tag{2.6}$$

$$\rho LW = \frac{z_B - z_C}{z_B - z_C + 50}(\sigma T_B{}^4 - LW_+^{\downarrow}), \tag{2.7}$$

$$\rho SW = 0.004(z_B - z_C) + \frac{6.25 \times 10^4}{z_B - z_C}\left\{1 - \exp\left[-\frac{(z_B - z_C)^2}{2.5 \times 10^6}\right]\right\}, \tag{2.8}$$

$$\begin{aligned}
&\left\{\beta\left[1 - \left(\frac{z_C}{z_B}\right)^2\right] + \left(\frac{z_C}{z_B}\right)^2\right\}(\overline{w'h'})_B - \left\{\epsilon\left[1 - \left(\frac{z_C}{z_B}\right)^2\right] + (1 - \epsilon\delta)\left(\frac{z_C}{z_B}\right)^2\right\}L\overline{w'(q' + l')}_B \\
&+ \left\{\beta\left(\frac{z_B - z_C}{z_B}\right)^2 + \left[1 - \left(\frac{z_B - z_C}{z_B}\right)^2\right]\right\}(\overline{w'h'})_S \\
&- \left\{\epsilon\left(\frac{z_B - z_C}{z_B}\right)^2 + (1 - \epsilon\delta)\left[1 - \left(\frac{z_B - z_C}{z_B}\right)^2\right]\right\}L(\overline{w'q'})_S + \frac{1 - k}{k} \\
&\times \min\left\{\begin{array}{c} \beta(\overline{w'h'})_B - \epsilon L\overline{w'(q' + l')}_B \\ \left[\frac{z_B - z_C}{z_B}(\overline{w'h'})_S + \frac{z_C}{z_B}(\overline{w'h'})_B\right] - (1 - \epsilon\delta)L\left[\frac{z_B - z_C}{z_B}(\overline{w'q'})_S + \frac{z_C}{z_B}\overline{w'(q' + l')}_B\right] \\ (\overline{w'h'})_S - (1 - \epsilon\delta)L(\overline{w'q'})_S \end{array}\right\} = 0,
\end{aligned} \tag{2.9}$$

$$\frac{L\Delta(q + l)}{\Delta h}(\overline{w'h'})_B - L\overline{w'(q' + l')}_B = \frac{L\Delta(q + l)}{\Delta h}LW, \tag{2.10}$$

$$\frac{dh_M}{dt} = \frac{(\overline{w'h'})_S - (\overline{w'h'})_B + SW}{z_B}, \tag{2.11}$$

$$\frac{d(q + l)_M}{dt} = \frac{(\overline{w'q'})_S - \overline{w'(q' + l')}_B}{z_B}, \tag{2.12}$$

$$\frac{dz_B}{dt} = -Dz_B + \frac{LW - (\overline{w'h'})_B}{\Delta h}. \tag{2.13}$$

TABLE 1. Dependent variables, constants and externally specified parameters of the model.

Dependent variables		Constants		Externally specified parameters	
Cloud-top height	z_B	See (2.15)	b	Large-scale divergence	D
Cloud-base height	z_C	Specific heat at constant pressure	c_p	Wind speed	V
Mixed-layer moist static energy	h_M	Gravity	g	Transfer coefficient	C_T
Mixed-layer total water mixing ratio	$(q + l)_M$	Scale height	H	Saturation moist static energy at sea surface temperature and pressure	h_S^*
Surface moist static energy flux	$(\overline{w'h'})_S$	Entrainment parameter	k		
Cloud-top moist static energy flux	$(\overline{w'h'})_B$	Latent heat of condensation	L		
Surface water vapor flux	$(\overline{w'q'})_S$	See (2.21)	β	Saturation mixing ratio at sea surface temperature and pressure	q_S^*
Cloud-top total water flux	$\overline{w'(q'+l')}_B$	See (2.21)	γ		
Cloud-top moist static energy jump	Δh	See (2.18)	δ	Moist static energy just above cloud top	h_+
Cloud-top total water jump	$\Delta(q + l)$	See (2.21)	ϵ		
Cloud-top temperature	T_B	Density	ρ	Water vapor mixing ratio just above cloud top	q_+
Longwave cooling	LW	Stefan-Boltzmann constant	σ	Downward longwave flux just above cloud top	$LW_+^\downarrow$
Shortwave heating	SW				

Eqs. (2.1) and (2.2) are bulk aerodynamic formulas for the surface fluxes of moist static energy h and water vapor mixing ratio q. The transfer coefficient C_T is given by

$$C_T = (1 + 0.07V) \times 10^{-3}, \qquad (2.14)$$

(for V in m s^{-1}) as suggested by Deacon and Webb (1962). It can be seen from the form of (2.1) and (2.2) that the surface fluxes are proportional to wind speed and to the difference between the saturation value at the sea surface temperature and pressure and the mixed-layer value.

Cloud base z_C is expressed in (2.3) as a function of the air-sea differences in h and q, the scale height H, and two dimensionless constants γ and b, where γ is given in (2.21) and b is given by

$$b = \frac{RT}{c_p}\left(\frac{\partial q^*}{\partial T}\right)_p + p\left(\frac{\partial q^*}{\partial p}\right)_T$$
$$= \kappa\epsilon\gamma + p\left(\frac{\partial q^*}{\partial p}\right)_T. \qquad (2.15)$$

Eq. (2.3) is an expression for the level at which the atmosphere will become saturated, i.e., where $q^* = (q + l)_M$. The constant b (b is an increasing function of reference temperature and a decreasing function of reference pressure) is simply the lapse rate of q^*.

Eqs. (2.4) and (2.5) are the cloud top jumps in moist static energy and total water mixing ratio. Note that the model does not consider any cloud-top jump in wind velocity. This omission eliminates any effects that possible cloud-top shear instability may have on the depth of the layer. The magnitude of any such effects is not known. The temperature just below cloud top is given by (2.6). Cloud-top temperature is determined by following a dry adiabat to cloud base and a moist adiabat from there to cloud top. The first two terms on the right-hand side give the surface air temperature, while the third and fourth terms give the temperature difference between the air at the surface and the air at cloud top.

Eqs. (2.7) and (2.8) constitute the longwave and shortwave radiation parameterizations. We assume that all of the longwave cooling occurs at cloud top and hence appears in the cloud-top jump condition (2.13), while all of the shortwave heating occurs in the mixed layer and hence appears in the mixed-layer budget (2.11). Recognizing that the longwave cooling of a thin cloud layer approaches zero as the thickness approaches zero, the idealized cooling is multiplied by a depth-dependent longwave emissivity. The function chosen for the longwave emissivity, $(z_B - z_C)/(z_B - z_C + 50)$ (where the thickness is in meters), is a compromise among a number

TABLE 2. Constants and temperature-pressure-dependent parameters. Values given in the right hand column are simply meant to be typical.

Constants	Reference temperature-pressure-dependent parameters
$c_p = 1004.52$ J kg^{-1} K^{-1}	$b = 0.0359$
$g = 9.8$ m s^{-1}	$H = 8307$ m
$k = 0.2$	$L = 2.47 \times 10^6$ J kg^{-1}
$\delta = 0.608$	$\beta = 0.533$
$\sigma = 5.67 \times 10^{-8}$ W m^{-2} K^{-4}	$\gamma = 1.34$
	$\epsilon = 0.115$
	$\rho = 1.22$ kg m^{-3}

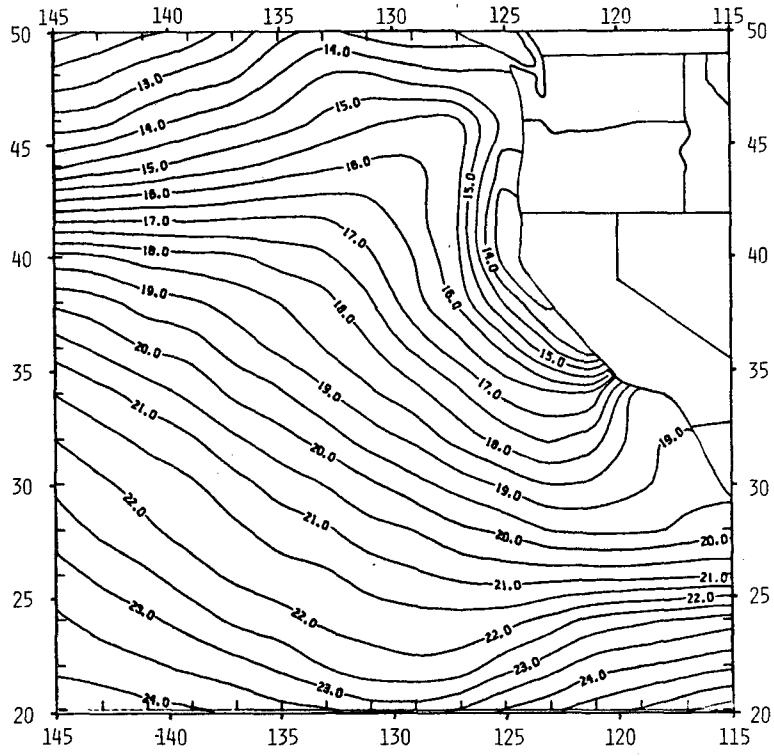

FIG. 4. Input field of sea surface temperature (°C).

of theoretical and observational curves, as discussed in WS.

In developing the function describing the dependence of shortwave absorption on cloud thickness the general approach of Deardorff (1976) was followed. He presented the shortwave radiative flux difference (W m^{-2}) across the cloud layer as

$$\rho SW = 0.004(z_B - z_C) + 0.025\lambda\{1 - \exp[-(z_B - z_C)/\lambda]\}, \quad (2.16)$$

where λ is the absorption length in meters. The absorption length should decrease as the liquid water content increases. A brief discussion of this problem can be found in Oliver *et al.* (1978), from which the approximate relation $\lambda \approx 500/\bar{l}$ m is derived, where $\bar{l}$ is the average liquid water mixing ratio of the cloud (g kg^{-1}). Coupling this with Neiburger's (1949) observation that $\bar{l} \approx (z_B - z_C)/5000$ g kg^{-1} leads directly from (2.16) to (2.8).

Experiments discussed in WS have shown that the placement of shortwave heating in the cloud layer rather than at cloud-top results in a more realistic simulation of the diurnal behavior of the stratocumulus-topped mixed layer. The fact that shortwave radiation is absorbed over a relatively deep layer of cloud served as the impetus for testing the change. Placement of up to a third of the shortwave at cloud top made no significant difference in diurnal results from those obtained with all of the shortwave heating in the mixed layer.

The entrainment relation (2.9) is derived from

$$\frac{k}{z_B}\int_0^{z_B} \overline{w's_v'}dz + \tfrac{1}{2}(1 - k)(\overline{w's_v'})_{\min} = 0, \quad (2.17)$$

which is a weighted ($0 \leq k \leq 1$) average of Lilly's maximum ($k = 1$) and minimum ($k = 0$) entrainment conditions. For this study, k is specified as 0.2. Further discussion of k and its effects on the model's solutions may be found in Section 2 of Schubert *et al.* (1979a). Including the effects of both water vapor and liquid water on buoyancy, the virtual dry static energy s_v is defined as

$$s_v = s + c_pT(\delta q - l), \quad (2.18)$$

where $\delta = 0.608$ and T is a constant reference temperature. By the definition of γ [Eq. (2.21)],

$$(1 + \gamma)L\overline{w'q'} = \gamma\overline{w'h'} \quad \text{for} \quad z_C < z < z_B, \quad (2.19)$$

and the turbulent flux of virtual dry static energy may be written

$$\overline{w's_v'} = \begin{cases} \beta\overline{w'h'} - \epsilon L\overline{w'(q' + l')}, & z_C < z < z_B \\ \overline{w'h'} - (1 - \epsilon\delta) \times L\overline{w'(q' + l')}, & 0 < z < z_C, \end{cases} \quad (2.20)$$

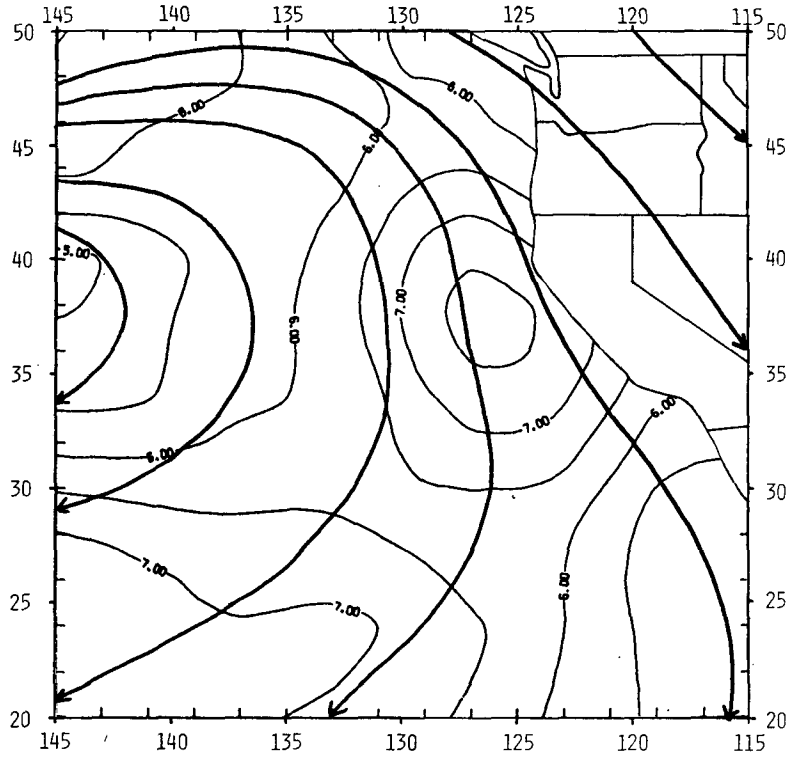

FIG. 5. Input field of wind speed V (m s^{-1}) and resultant streamlines.

where

$$\beta = \frac{1 + \gamma\epsilon(\delta + 1)}{1 + \gamma}, \quad \gamma = \frac{L}{c_p}\left(\frac{\partial q^*}{\partial T}\right)_p,$$

$$\epsilon = \frac{c_p T}{L}. \tag{2.21}$$

Substituting (2.20) into (2.17) and making use of the linear height dependence of $\overline{w'h'}$ and $\overline{w'(q' + l')}$, we obtain (2.9). Since (2.20) indicates that the s_v flux is linear below cloud and within the cloud, with a discontinuity at cloud base, it might seem that the minimum s_v flux appearing in (2.17) could occur at one of four locations: at the surface, just below cloud base, just above cloud base or at cloud top. It has been demonstrated by Schubert *et al.* (1979a) that the flux increases across cloud base, and thus the minimum cannot occur at z_{C+}. The three lines inside the large brackets in (2.9) correspond to the three remaining possible solutions.

Eq. (2.10) expresses the consistency relation between cloud top jumps and fluxes. This relation is obtained by eliminating $(dz_B/dt - w_B)$ between the cloud top jump conditions

$$\left(\frac{dz_B}{dt} - w_B\right)\Delta h + \overline{w'h'_B} = LW, \tag{2.22}$$

$$\left(\frac{dz_B}{dt} - w_B\right)\Delta(q + l) + \overline{w'(q' + l')}_B = 0. \tag{2.23}$$

The remaining three equations, (2.11)–(2.13), are predictive equations for the mixed-layer values of h and $(q + l)$, and for the cloud top z_B. Eqs. (2.11) and (2.12) are simply mixed-layer budget equations, while (2.13) is another form of the cloud-top jump condition (2.22), under the assumption that the cloud-top subsidence $-w_B$ is given by the large-scale divergence times the cloud-top height.

Given a knowledge of sea surface temperature, winds and divergence, as well as upper level (i.e., above the mixed layer) q, h and $LW_+^\downarrow$ profiles, the system (2.1)–(2.13) may be numerically integrated as follows:

1) Assume initial conditions for h_M, $(q + l)_M$ and z_B.
2) Compute the surface fluxes of h and q from (2.1) and (2.2).
3) Compute cloud base from (2.3).
4) Compute the cloud top jumps of h and $(q + l)$ from (2.4) and (2.5).
5) Compute the cloud-top temperature from (2.6), then the longwave and shortwave radiative effects from (2.7) and (2.8).
6) Solve the system (2.9) and (2.10) for the cloud-top fluxes $(\overline{w'h'})_B$ and $L\overline{w'(q' + l')}_B$.
7) Predict new values of h_M, $(q + l)_M$, and z_B from (2.11)–(2.13).
8) Return to step 2.

The solution of (2.9) and (2.10) is not trivial. The form of (2.9) shows that in order for a solution to be found, the location of the minimum s_v flux must be known. From (2.20), it can be seen that this means

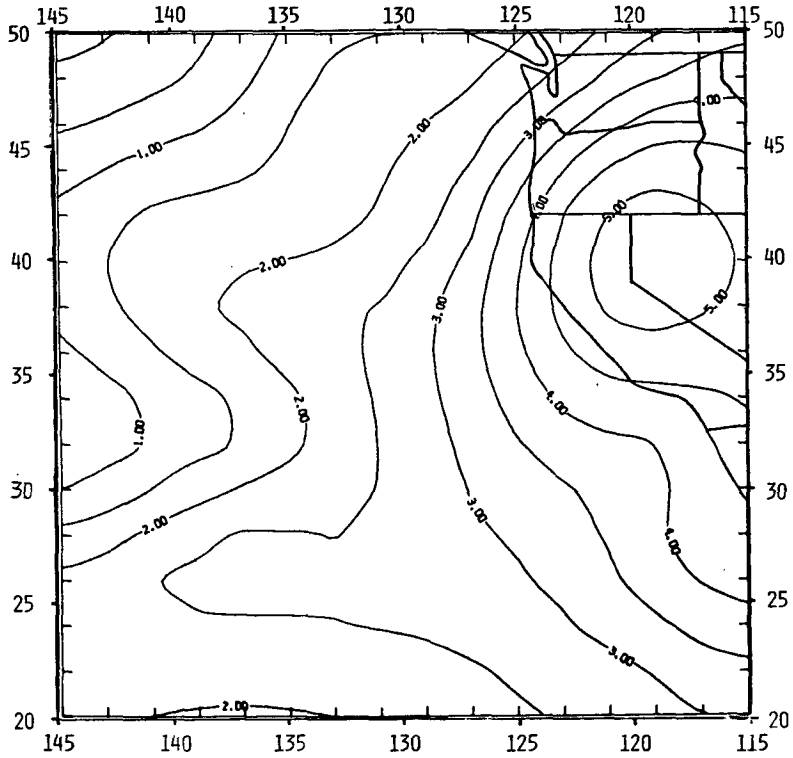

FIG. 6. Input field of large-scale divergence D (10^{-6} s^{-1}).

that the fluxes of h and $(q + l)$ at cloud top must also be known. To solve (2.9) and (2.10), therefore, we assume that the minimum occurs at each of the three possible levels, solve the matrix, and, in each case, use (2.20) to check the location of the minimum. In all cases we have found that a solution exists, and in those few cases where more than one solution exists, we have found that by using the solution with the minimum closer to the surface, the integration proceeds in an orderly manner.

3. Procedure and input data

The model outlined in Section 2 was applied to the region bounded by 145°W, 115°W, 40°N[3] and 20°N. Given surface wind speed and direction over this region, and given a distance increment and an initial position on the inflow part of the boundary, one can calculate a sequence of positions and time intervals along a trajectory[4] using the method of great circle navigation. Then the model equations can be integrated along the trajectory. By considering many such trajectories, two dimensional fields of all the dependent variables of the model can be constructed.

An examination of the model equations (Section 2) reveals that each trajectory calculation requires specification of the constants c_p, g, k, δ, σ, the reference temperature-pressure-dependent parameters $b, H, L, \beta, \gamma, \epsilon, \rho$, mixed-layer input data h_S^*, q_S^*, V, D, C_T, free atmosphere input data h_+, q_+, $LW_+^\downarrow$, and initial conditions on z_B, h_M, and $(q + l)_M$. Values assumed for the constants are listed in the left column of Table 2. For those parameters which require a reference temperature and/or pressure, a reference temperature 4.5 K colder than the sea surface temperature, and a reference pressure 4.5 kPa less than the assumed surface pressure (102 kPa) were used. Typical values of these quantities are listed in the right column of Table 2.

The mixed-layer input quantities h_S^*, q_S^*, V, D and C_T can be determined from sea surface temperature, wind speed and direction. July mean sea surface temperature data were obtained from the monthly mean North Pacific charts of LaViolette and Seim (1969). This sea surface temperature field is shown in Fig. 4. For wind speed, wind direction and large-scale divergence the mean wind data for July of 1961 through 1974 as presented by Miller and Stevenson (1974)[5] were used. These data are given as average

[3] Calculations were also made with the northern boundary at 50°N. The results (not shown) were less satisfactory probably because this is outside the stratocumulus region (see Figs. 1 and 2).

[4] Under the assumption of steady-state winds made here, the terms trajectory and streamline are interchangeable. In the more general case, trajectories would be calculated, so we use that term.

[5] Miller, F. R., and M. R. Stevenson, 1974: Comparison of cloud top temperatures from satellites and sea surface temperatures along Baja California. Paper presented at V Congreso Nacional de Oceanografia, October 1974. [Available from the authors at Scripps Institution of Oceanography, LaJolla, California.]

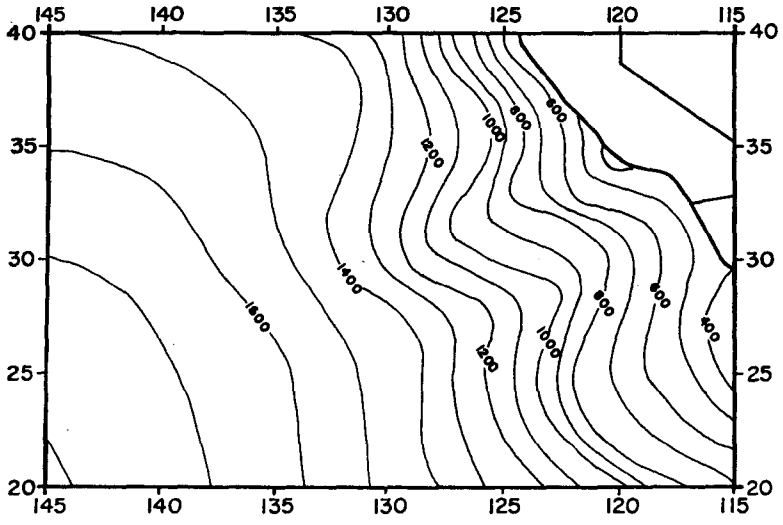

FIG. 7. June–September cloud-top data (m) after Neiburger *et al.* (1961).

values over 5° × 5° areas and display the same qualitative features as the data of Neiburger *et al.* (1961). The wind speed field and the resultant streamlines are shown in Fig. 5, and the large-scale divergence in Fig. 6. It should be noted that this wind data has somewhat less than half the spatial resolution of the sea surface temperature data.

To determine h_+, q_+ and $LW_+^{\downarrow}$, mean atmosphere data for July of 1967 through 1970 were obtained from U.S. Department of Commerce (1967–1970a) for the rawinsonde stations Quillayute, Oakland and San Diego, and from U.S. Department of Commerce (1967–1970b) for Ships P and N. These data were averaged over the four Julies, resulting in July soundings of temperature and dew point temperature as functions of height. After computing h and q from the temperature and dew-point temperature at each station, and after setting aside low-level values which contained the effects of the boundary layer and the inversion layer, functions of height and latitude were fit to the data. The resulting equations are

$$h_+ = 242.29 + 94.34 \cos\phi + (4.72 - 3.93 \cos\phi) \times 10^{-3} z_B \text{ [kJ kg}^{-1}\text{]}, \quad (3.1)$$

$$q_+ = \begin{cases} \dfrac{20}{z_B + 300 + 30\phi} - 0.0016 \text{ [g g}^{-1}\text{]}, & z_B \geqslant 1500 \\ \dfrac{20}{1800 + 30\phi} - 0.0016 - (0.42 - 2.96 \cos\phi) \times 10^{-6}(1500 - z_B), & z_B < 1500, \end{cases} \quad (3.2)$$

where ϕ is latitude in degrees. The longwave radiative transfer model of Cox (1973) was then used to calculate the vertical profiles of downward longwave radiative flux. The inputs to this radiation model are temperature, pressure, and water vapor mixing ratio. Straight lines were fit to the calculated radiative flux profiles as functions of height and latitude, with the result that

$$LW_+^{\downarrow} = 60.23 + 339.9 \cos\phi - (1.084 + 2.974 \cos\phi) \times 10^{-2} z_B \text{ [W m}^{-2}\text{]}. \quad (3.3)$$

The final step in preparation for the numerical integration is the initialization of z_B, h_M and $(q + l)_M$. Cloud-top height z_B was initialized (i.e., its value along 40°N was specified) from the observations of Neiburger *et al.* (1961), which are shown in Fig. 7. The initial $(q + l)_M$ and h_M were obtained by assuming that there is no initial air-sea temperature difference [i.e., $(s - Ll)_M = c_p T_S$ at $t = 0$] and that initially the cloud-base height is half the cloud-top height. Then, using (2.3) we can write

$$\left.\begin{aligned} (q + l)_M &= q_S^* - \frac{b z_B}{2H} \\ h_M &= c_p T_S + L(q + l)_M \end{aligned}\right\} \quad \text{at} \quad t = 0. \quad (3.4)$$

4. Results

In this section, the results of the numerical integration of the model will be presented and com-

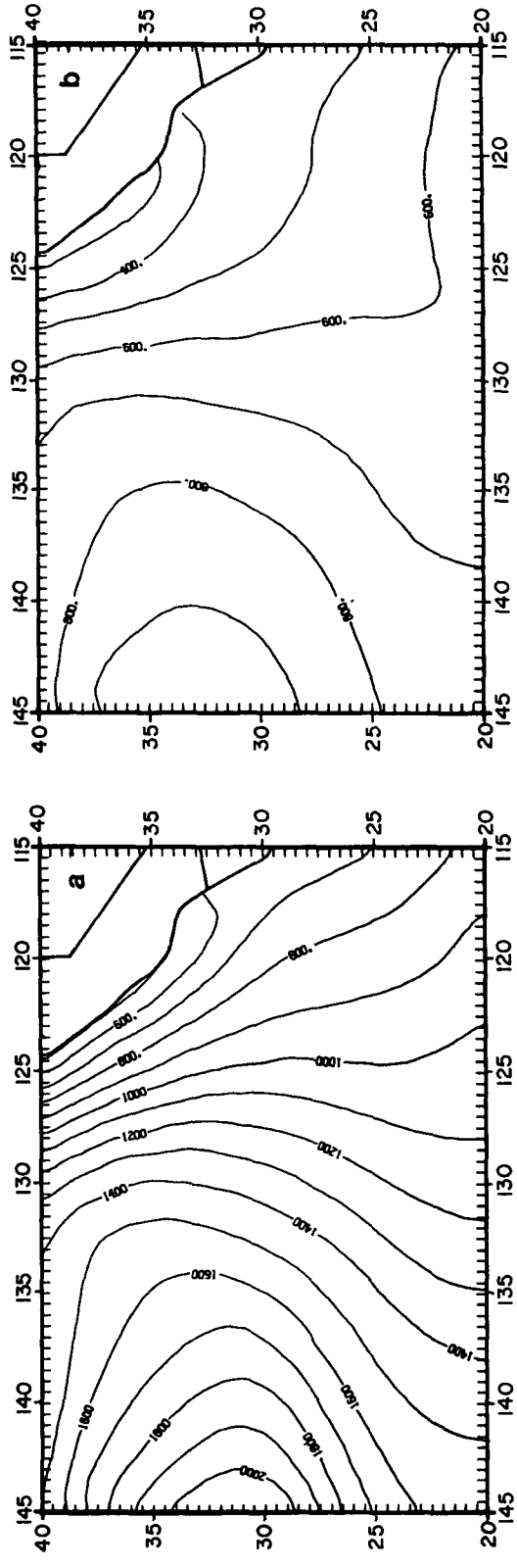

FIG. 8. Model results of (a) cloud-top height (m); (b) cloud-base height (m).

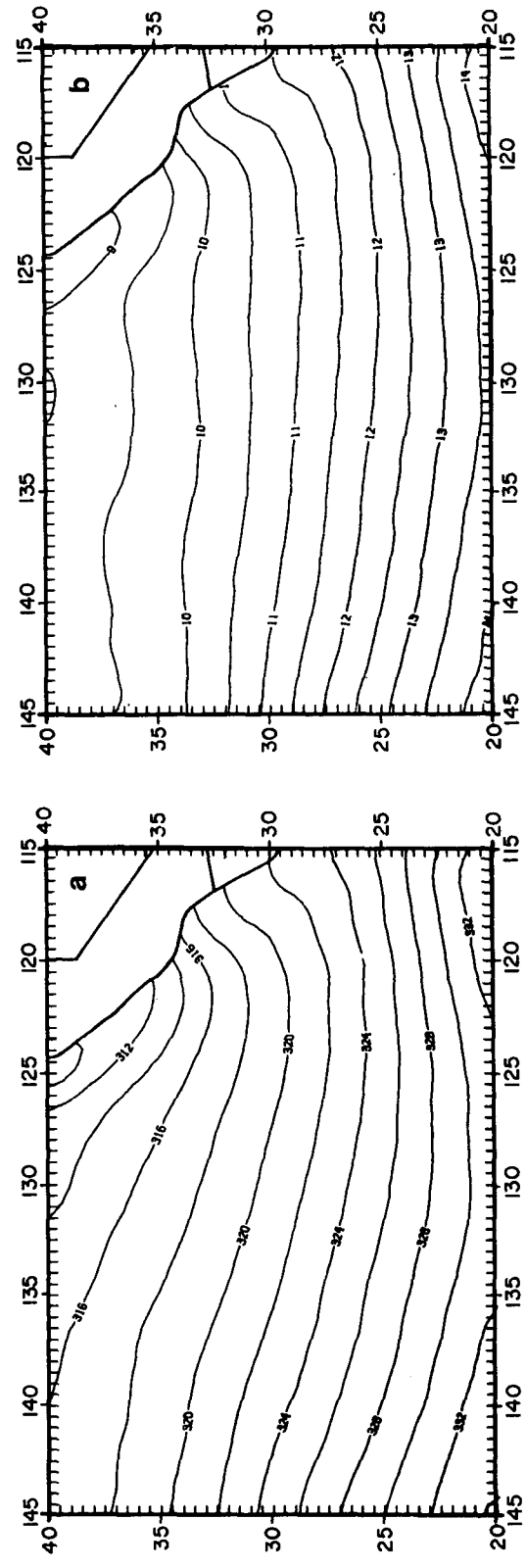

FIG. 9. Mixed-layer values of (a) moist static energy (kJ kg^{-1}); (b) total water mixing ratio (g kg^{-1}).

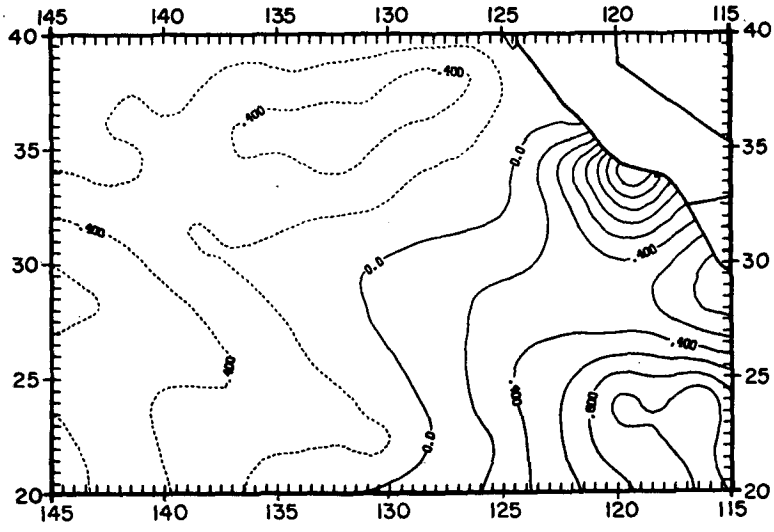

FIG. 10. Sea surface temperature minus air temperature (°C).

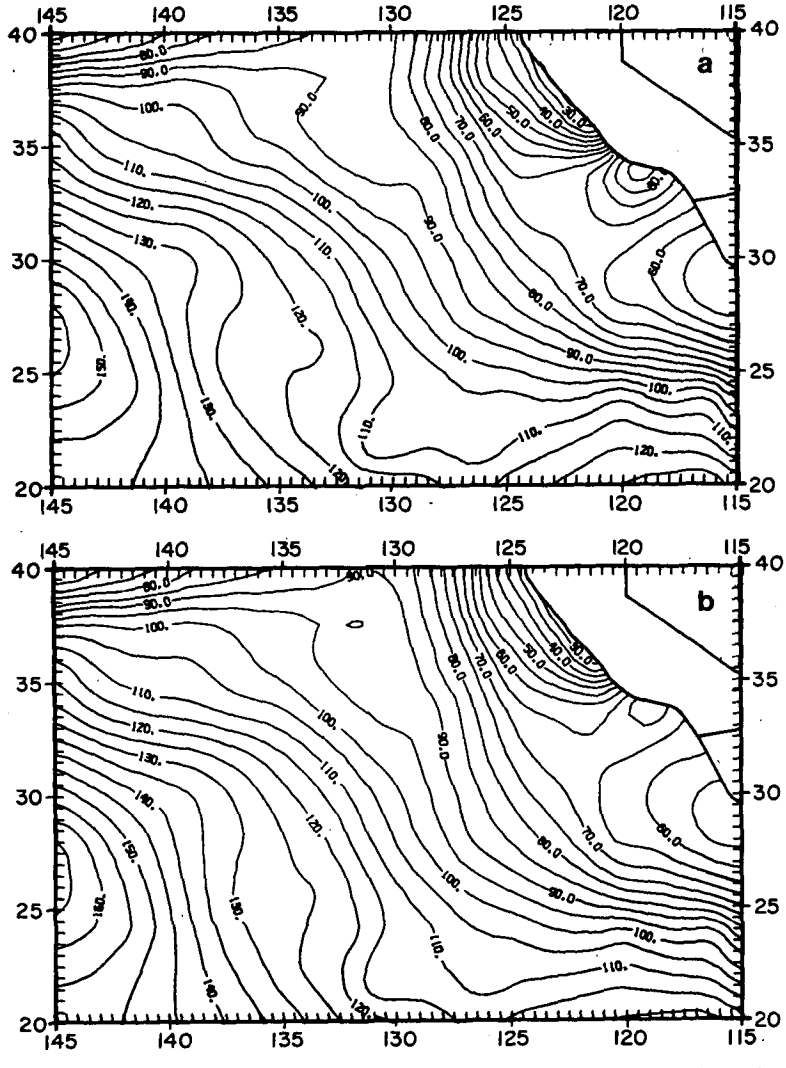

FIG. 11. Surface fluxes of (a) moist static energy (W m^{-2}); (b) water vapor mixing ratio (W m^{-2}).

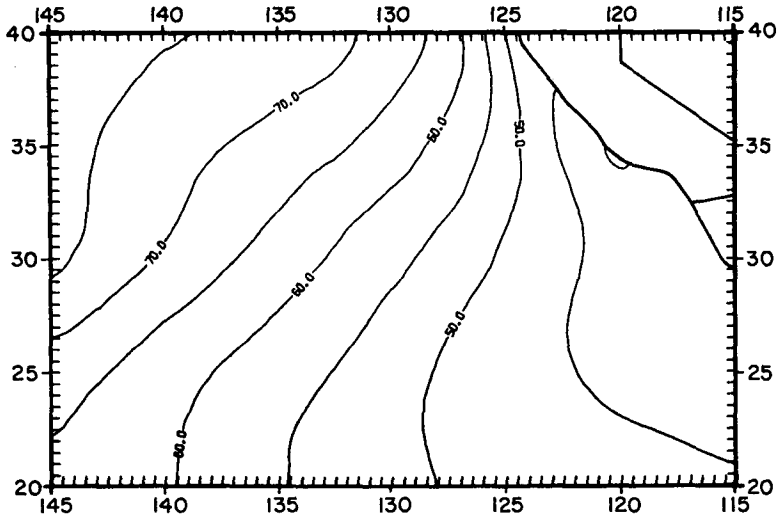

FIG. 12. Longwave radiative flux divergence across cloud top (W m^{-2}).

pared with observations. The results presented here should be interpreted with caution, since the large-scale inputs already discussed are only estimates of the climatological conditions. Day-to-day variations in these input fields may be quite large.

a. Results of the numerical integrations

The initialization of the trajectories was made every degree of longitude along 40°N from 145°W to 116°W, for a total of 30 trajectories. The distance increment along each trajectory was 5 km.

The results for cloud top height and cloud base height are shown in Fig. 8. It can be seen (Fig. 8a) that z_B is nearly constant along the coast. Away from the coast, cloud tops rise to the west, in accordance with the lower divergence there. As noted by Schubert *et al.* (1979a), cloud-top height in the horizontally homogeneous case is roughly inversely proportional to divergence.

Cloud base height (Fig. 8b) is closely related to sea surface temperature, as can be seen by comparing Figs. 4 and 8b. Eq. (2.3), which governs the cloud-base height, can be used to examine the effects of changing sea surface temperature on z_C. It turns out that changes in the reference temperature dependent parameters γ, H, L and b cause only small changes in z_C. In addition, q_s^* and h_s^* change in a related manner such that the difference in (2.3) is unchanged. This arises from the fact that $\gamma/L\Delta h_s^* = (1 + \gamma)\Delta q_s^*$. When sea surface temperature rises, the rising h_s^* and q_s^* cause larger surface fluxes of h and q, which result in increases in h_M and $(q + l)_M$. Model results to be presented later indicate that $L(q + l)_M$ increases more slowly than h_M in the region off the central California coast, which means that the air temperature rises (as expected). Therefore, cloud base rises in this area.

The cloud thickness field (not shown) closely follows that of the cloud-top height field, further illustrating that the response of cloud-top height is larger than that of cloud-base height. Almost the entire cloud layer is thick enough that the blackbody assumption for longwave emissivity would be reasonable. In terms of shortwave absorption, however, (2.8) shows that SW may vary by a factor of 4 over the range of thicknesses produced by the integrations.

The mixed-layer values of both moist static energy and total water mixing ratio closely parallel the sea surface temperature. Isolines of h_M and $(q + l)_M$ are shown in Fig. 9. Near the central California coast, h_M increases more rapidly than $L(q + l)_M$ along the trajectories. This indicates that the air is warming. This warming is somewhat slower than that of sea surface temperature. Thus, the sea-air temperature difference $(T_s - T_{\text{air}})$ becomes positive, as shown in Fig. 10. Note that, as discussed in Section 4 of Schubert *et al.* (1979a), if the mixed layer were in a horizontally homogeneous steady state, $T_s - T_{\text{air}}$ would be slightly negative everywhere.

Surface turbulent fluxes of moist static energy and water vapor mixing ratio are shown in Fig. 11. The general shape of these fields is related to wind speed and sea surface temperature. Cloud-top fluxes of moist static energy, total water mixing ratio, and longwave radiation are interrelated in a complex manner. The first two (not shown) exhibit characteristics similar to the surface fluxes, although their magnitudes are roughly half of the surface fluxes.

The longwave radiative flux difference across cloud top, which represents the basic driving force behind this type of convection, is shown in Fig. 12. Its variation is closely related to that of z_B.

Fluxes of virtual dry static energy are shown in Fig. 13. These fluxes are simply linear combinations of the moist static energy and total water fluxes,

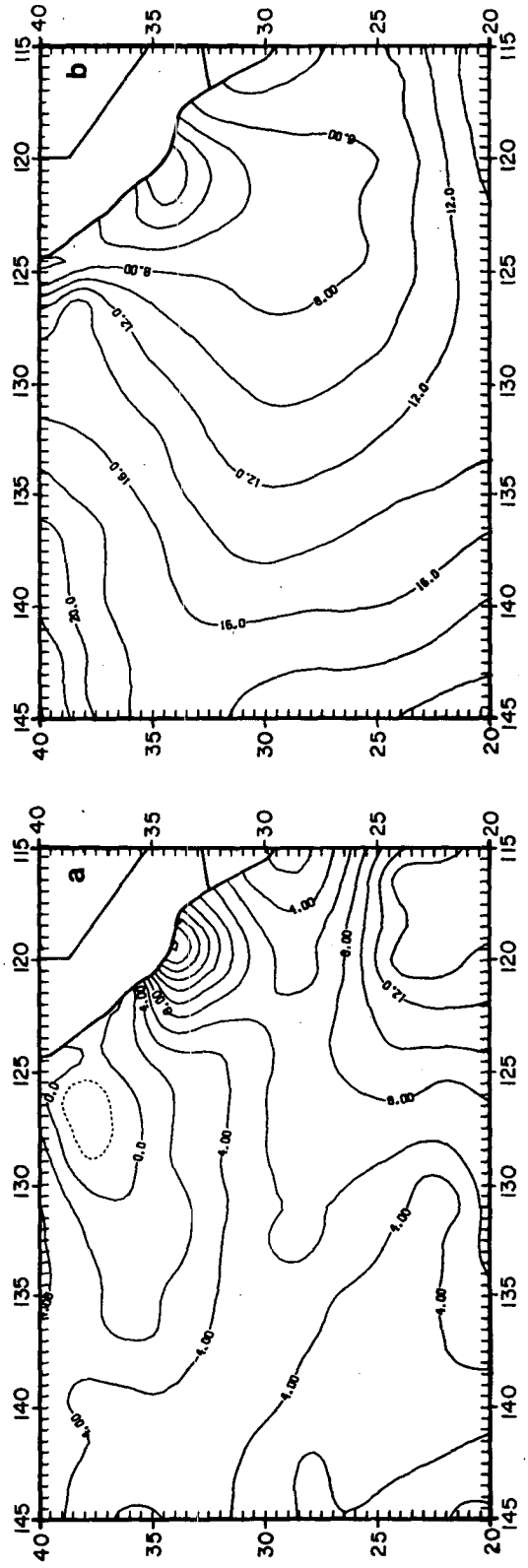

FIG. 13. Fluxes of virtual dry static energy (W m^{-2}) for (a) surface, (b) cloud top.

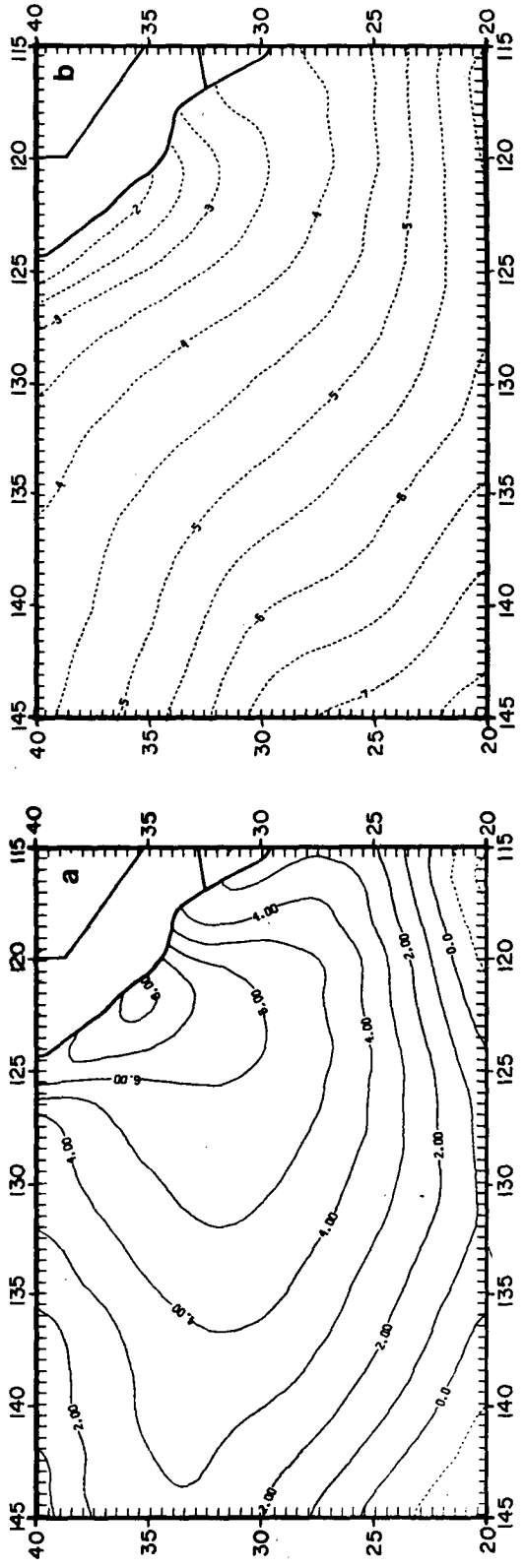

FIG. 14. Cloud-top jumps of (a) moist static energy (kJ kg^{-1}) and (b) total water mixing ratio g kg^{-1}).

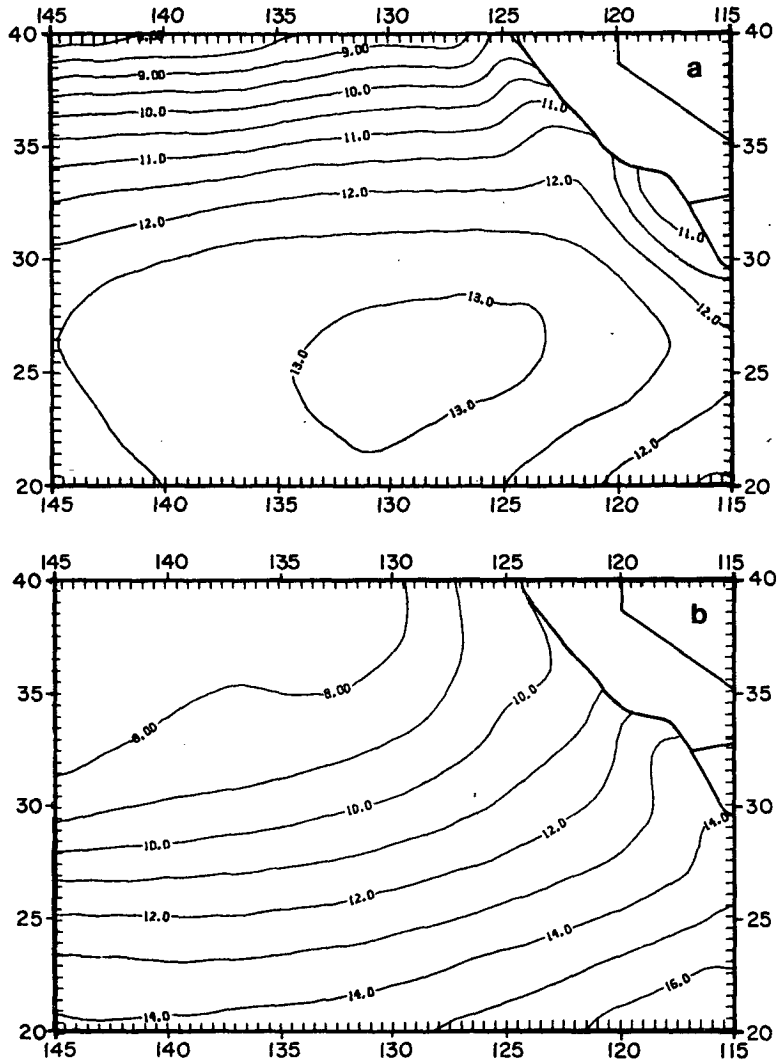

FIG. 15. (a) Magnitude of inversion and (b) cloud-top temperature (°C).

as given by Eq. (2.20). As a result, the surface flux is similar in appearance to the other surface fluxes and the air-sea temperature difference, and the cloud-top flux is similar to the other cloud-top fluxes. The fluxes at the subcloud/cloud interface are not shown, but the flux just below cloud base is always negative.

Cloud-top jumps of moist static energy and total water mixing ratio are shown in Fig. 14. The air above the mixed layer is in all cases warmer and drier than the air below the inversion. Thus, $\Delta(q + l)$ is always negative and Δh, it turns out, is almost always positive. According to Lilly (1968), in the small areas where Δh is negative (southwestern and southeastern corners), the results are questionable, since negative Δh implies negative buoyancy (hence instability) of a parcel brought from above the mixed layer across the inversion. Lilly's argument does not include virtual temperature effects. Recently, Randall (1980a) and Deardorff (1980a) have presented more exact arguments which show that a somewhat negative Δh is still stable. In any event, the model seems to produce negative Δh near the southern boundary, which is where Fig. 1 indicates that the stratocumulus regime breaks up.

The temperature difference from base to top of inversion is shown in Fig. 15a and the cloud-top temperature in Fig. 15b. The latitudinal dependence of above-inversion temperature can be seen to play a significant role in the inversion strength.

The quantity $\rho(dz_B/dt - w_B)$ is just the net mass flowing into the mixed layer per unit horizontal area per unit time, i.e., the net mass entrainment at cloud top. This entrainment is shown in Fig. 16.

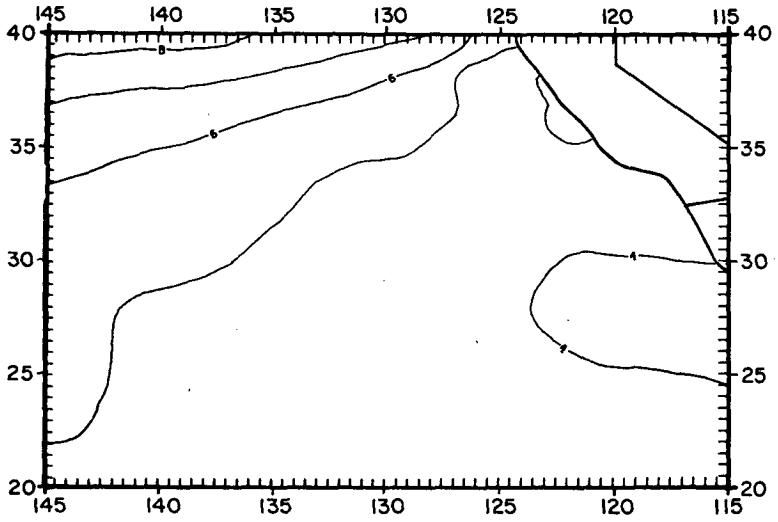

FIG. 16. Cloud-top mass entrainment (g m^{-2} s^{-1}).

b. Comparison with observations

Only three of the several fields presented earlier in this section are recorded in the observations of Neiburger *et al.* (1961). These three are cloud-top height, temperature at cloud top, and the increase of temperature across the inversion. The observations are for the whole summer.

The cloud-top temperatures observed by Neiburger *et al.* are shown in Fig. 17. The cloud-top height field was previously shown in Fig. 7.

Cloud-top heights (Figs. 7 and 8a) show a basic similarity in the northern portions of the grid, as would be expected from the initialization scheme. The fields are similar in that isolines run more-or-less north to south and there is an increase in height away from the coast. Model isolines tend to follow the trajectories in the southwest, as would be expected from the long memory of z_B. In general, though, the comparison is good.

Comparison of Figs. 15b and 17 indicates that there is a reasonable agreement between the model results and observations for cloud-top temperature. The general shape of the model results plot is the same as the observations, with a maximum to the southeast and a minimum to the northwest.

Inversion magnitude results (not shown) compare less favorably with the observations. One possible explanation is that this parameter is difficult to measure in that the top of an inversion is often hard to determine. A second, and perhaps more com-

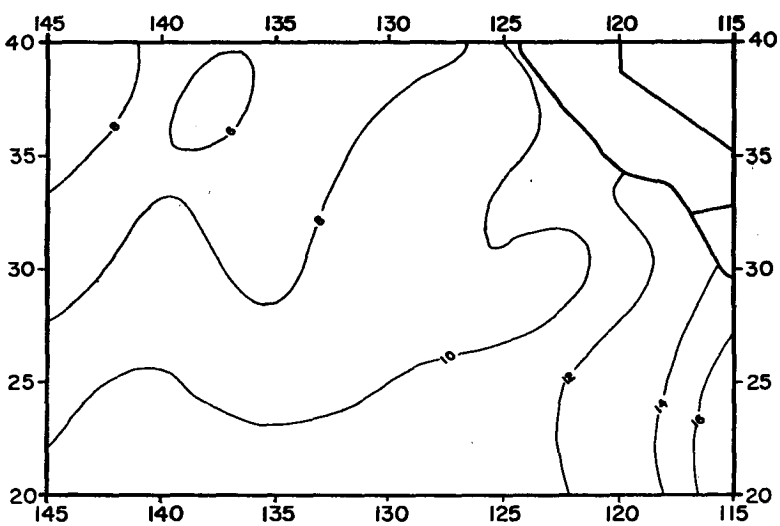

FIG. 17. Observations of cloud-top temperture (°C) after Neiburger *et al.* (1961).

pelling reason for the discrepancy is that the model assumes that any inversion has essentially zero thickness, which has the effect of increasing the magnitude of the inversion.

5. Concluding remarks

It was demonstrated in Section 4 that the model's reproduction of the observed mixed-layer features is adequate in many, but not all, respects. There are, however, a number of things which should be kept in mind when considering these results.

In the first place, it was noted above that the Neiburger *et al.* observations cover the period June–September, while the input data for the model were July only. Neiburger *et al.* (1961) indicate in their data that, at 16 of the 18 land or ship stations whose data were employed, the July incidence of inversion is greater than the summer average. This suggests the possibility that July inversions may have somewhat different characteristics than the all-summer average data presented.

A second basis for dissimilarity lies in the initialization procedure. Initialization of cloud base and air-sea temperature difference is hampered by the lack of observational data. Better initialization of these parameters could contribute to improving the model results.

Problems at the coastline constitute a third source of error. In this case, the model has no provisions for landfall, so the results along the coast may be worse than those over open ocean.

Finally, it must be kept in mind when considering any climatologically-based study that most atmospheric systems are nonlinear. Schubert *et al.* (1979a) have demonstrated that the steady-state results of this model are decidedly nonlinear. This is of particular importance when trying to reproduce mean observations from mean data. It is quite likely that the stratocumulus field on any given day would be considerably different from either the model results presented here or the observational evidence presented by Neiburger *et al.* Furthermore, the length of some of the trajectories used in the model calculations is such that the traverse time for a parcel of air could be as much as several days, a time period during which many changes would surely take place in the basic synoptic pattern.

For these reasons, the model results should not necessarily be expected to closely match the observed stratocumulus regime, nor should either of the two be expected to correspond to any single day's convection. The fact that the model approximately reproduces the observations speaks in its favor.

Possible improvements of the model include the incorporation of day-to-day changes in the external fields, such that the trajectories would become true trajectories rather than steady-state streamlines. This could then allow the model to be used on a daily basis compared to actual synoptic conditions. This opens the door to the possibility of using the model as a forecasting tool, especially if a momentum budget were added, such that only the sea surface temperature and surface pressure would be specified. In addition, the imposition of a land-sea interface is probably required in order that the coastal convection be adequately modeled.

Acknowledgments. The authors wish to thank Drs. Stephen K. Cox and Eugene L. Maxwell for their critical review of this work, and Odilia Panella and Mary Niemczewski for their help in preparing the manuscript. The research reported here has been supported by the National Science Foundation through Grant ATM-7808125 and the Office of Naval Research through Grant N00014-C-79-0793.

REFERENCES

Asai, T., and K. Nakamura, 1978: A numerical experiment of airmass transformation processes over warmer sea, Part I: Development of a convectively mixed layer. *J. Meteor. Soc. Japan*, **56**, 424–434.

Cox, S. K., 1973: Infrared heating calculations with a water vapor pressure broadened continuum. *Quart. J. Roy. Meteor. Soc.*, **99**, 669–679.

Deacon, E. L., and E. K. Webb, 1962: Interchange of properties between the sea and air. *The Sea*, Vol. 1, M. N. Hall, Ed., Rockefeller Institute Press, p. 43.

Deardorff, J. W., 1976: On the entrainment rate of a stratocumulus-topped mixed layer. *Quart. J. Roy. Meteor. Soc.*, **102**, 563–582.

——, 1980a: Cloud top entrainment instability. *J. Atmos. Sci.*, **37**, 131–147.

——, 1980b: Stratocumulus-capped mixed layers derived from a three-dimensional model. *Bound.-Layer Meteor.*, **18**, 495–527.

——, and J. A. Businger, 1980: Comments on "Marine stratocumulus convection, Part I: Governing equations and horizontally homogeneous solutions". *J. Atmos. Sci.*, **37**, 481–482.

Kahn, P. H., and J. A. Businger, 1979: The effect of radiative flux divergence on entrainment of a saturated convective boundary layer. *Quart. J. Roy. Meteor. Soc.*, **105**, 303–306.

Kraus, H., and E. Schaller, 1978a: Steady-state characteristics of inversions capping a well-mixed PBL. *Bound.-Layer Meteor.*, **14**, 83–104.

——, and ——, 1978b: A note on the closure in Lilly-type inversion models. *Tellus*, **30**, 284–288.

LaViolette, P. E., and S. E. Seim, 1969: Monthly charts of mean, minimum, and maximum sea surface temperature in the North Pacific Ocean. SP-123, U.S. Naval Oceanographic Office, Washington, DC, 62 pp.

Lilly, D. K., 1968: Models of cloud-topped mixed layers under a strong inversion. *Quart. J. Roy. Meteor. Soc.*, **94**, 292–309.

——, and W. H. Schubert, 1980: The effects of radiative cooling in a cloud-topped mixed layer. *J. Atmos. Sci.*, **37**, 482–487.

Miller, D. B., and R. G. Feddes, 1971: Global atlas of relative cloud cover 1967–1970. Joint production by U.S. Dept. of Commerce and U.S. Air Force, Washington, D.C. [NTIS AD-739-434].

Moeng, C.-H., and A. Arakawa, 1980: A numerical study of marine subtropical stratus cloud layer and its stability. *J. Atmos. Sci.*, **37**, 2661–2676.

Neiburger, M., 1949: Reflection, absorption, and transmission of insolation by stratus clouds. *J. Meteor.*, **6**, 98–104.

——, D. S. Johnson and C. W. Chien, 1961: Studies of the structure of the atmosphere over the eastern Pacific Ocean in summer, I, The inversion over the eastern north Pacific Ocean. *Univ. Calif. Publ. meteor.*, **1**, 1–94.

Oliver, D. A., W. S. Lewellen and G. G. Williamson, 1978: The interaction between turbulent and radiative transport in the development of fog and low-level stratus. *J. Atmos. Sci.*, **35**, 301–316.

Randall, D. A., 1980a: Conditional instability of the first kind upside-down. *J. Atmos. Sci.*, **37**, 125–130.

——, 1980b: Entrainment into a stratocumulus layer with distributed radiative cooling. *J. Atmos. Sci.*, **37**, 148–159.

Schaller, E., and H. Kraus, 1981a: The role of radiation in an inversion-capped planetary boundary layer, Part I: The need for a detailed consideration of radiative processes. *Bound.-Layer Meteor.*, **20**, 485–495.

——, and ——, 1981b: The role of radiation in an inversion-capped planetary boundary layer, Part II: The internally interactive radiative-convective model. Submitted to *Bound.-Layer Meteor.*, **20**, 497–513.

Schubert, W. H., 1976: Experiments with Lilly's cloud-topped mixed layer model. *J. Atmos. Sci.*, **33**, 436–446.

——, J. S. Wakefield, E. J. Steiner and S. K. Cox, 1979a: Marine stratocumulus convection, Part I: Governing equations and horizontally homogeneous solutions. *J. Atmos. Sci.*, **36**, 1286–1307.

——, ——, —— and ——, 1979b: Marine stratocumulus convection, Part II: Horizontally inhomogeneous solutions. *J. Atmos. Sci.*, **36**, 1308–1324.

U.S. Dept. of Commerce, Environmental Science Services Administration, Environmental Data Service, 1967–70a: *Climatological Data, National Summary*, **18–21**, No. 7. [U.S. Govt. Printing Office].

——, 1967–70b: *Monthly Climatic Data for the World*, **20–23**, No. 7. [U.S. Govt. Printing Office].